

Testing Primordial Black Holes as Dark Matter through LISA

N. Bartolo^{a,b,c}, V. De Luca^d, G. Franciolini^d, M. Peloso^{a,b}, D. Racco^{d,e} and A. Riotto^d

^a *Dipartimento di Fisica e Astronomia “G. Galilei”, Università degli Studi di Padova, via Marzolo 8, I-35131 Padova, Italy*

^b *INFN, Sezione di Padova, via Marzolo 8, I-35131 Padova, Italy*

^c *INAF - Osservatorio Astronomico di Padova, Vicolo dell’Osservatorio 5, I-35122 Padova, Italy*

^d *Department of Theoretical Physics and Center for Astroparticle Physics (CAP)*

24 quai E. Ansermet, CH-1211 Geneva 4, Switzerland

^e *Perimeter Institute for Theoretical Physics, 31 Caroline St. N., Waterloo, Ontario N2L 2Y5, Canada*

Abstract

The idea that primordial black holes (PBHs) can comprise most of the dark matter of the universe has recently reacquired a lot of momentum. Observational constraints, however, rule out this possibility for most of the PBH masses, with a notable exception around $10^{-12}M_{\odot}$. These light PBHs may be originated when a sizeable comoving curvature perturbation generated during inflation re-enters the horizon during the radiation phase. During such a stage, it is unavoidable that gravitational waves (GWs) are generated. Since their source is quadratic in the curvature perturbations, these GWs are necessarily fully non-Gaussian. Their frequency today is about the mHz, which is exactly the range where the LISA mission has the maximum of its sensitivity. This is certainly an impressive coincidence. We show that this scenario of PBHs as dark matter can be tested by LISA by measuring not only the GW two-point correlator, but also the GW three-point correlator for which we study the LISA response functions and construct a suitable estimator to test the non-Gaussianity of GWs.

I. INTRODUCTION

The possible presence and composition of dark matter (DM) in our universe constitutes one of the open questions in physics [1]. The first direct observation of GWs generated by the merging of two $\sim 30M_{\odot}$ black holes [2] has increased the attention to the possibility that all (or a significant fraction of) the dark matter is composed by PBHs (see Refs. [3–6] and [7, 8] for recent reviews). Inflation and a mechanism to enhance the comoving curvature perturbation ζ [9–11] at scales smaller with respect to the CMB ones are the only ingredients needed by the simplest models describing the PBH formation without the request of any physics beyond the Standard Model. In fact, the perturbations themselves of the Standard Model Higgs may be responsible for the growing of the comoving curvature perturbations during inflation [12].

Perturbations generated during inflation are transferred to radiation through the reheating process after inflation. After they re-enter the horizon, a region collapses to a PBH if the density contrast (during the radiation era)

$$\Delta(\vec{x}) = \frac{4}{9a^2H^2} \nabla^2 \zeta(\vec{x}) \quad (1.1)$$

is larger than the critical value Δ_c which depends on the shape of the power spectrum [13]. The temperature at which the collapse takes place is

$$T_M \simeq 10^{-1} \left(\frac{106.75}{g_*} \right)^{1/4} \left(\frac{M_{\odot}}{M} \right)^{1/2} \text{ GeV}, \quad (1.2)$$

where we have normalized g_* to the effective number of the Standard Model degrees of freedom. We define the power spectrum of the comoving curvature perturbation as

$$\langle \zeta(\vec{k}_1) \zeta(\vec{k}_2) \rangle' = \frac{2\pi^2}{k_1^3} \mathcal{P}_{\zeta}(k_1), \quad (1.3)$$

where we used the prime to indicate the rescaled two point function without the $(2\pi)^3$ and the Dirac delta for the momentum conservation.

It is useful to define the variance of the density contrast as

$$\sigma_{\Delta}^2(M) = \int_0^{\infty} d \ln k W^2(k, R_H) \mathcal{P}_{\Delta}(k), \quad (1.4)$$

where we inserted a Gaussian window function $W(k, R_H)$ to smooth out the density contrast on scales given by the comoving horizon $R_H \sim 1/aH$ and the density contrast power spectrum

$$\mathcal{P}_{\Delta}(k) = \left(\frac{4k^2}{9a^2 H^2} \right)^2 \mathcal{P}_{\zeta}(k). \quad (1.5)$$

The mass fraction β_M indicating the portion of energy density of the universe collapsed into PBHs at the time of formation is

$$\beta_M = \int_{\Delta_c}^{\infty} \frac{d\Delta}{\sqrt{2\pi} \sigma_{\Delta}} e^{-\Delta^2/2\sigma_{\Delta}^2} \simeq \frac{\sigma_{\Delta}}{\Delta_c \sqrt{2\pi}} e^{-\Delta_c^2/2\sigma_{\Delta}^2}, \quad (1.6)$$

under the assumption of a Gaussian probability distribution. For the non-Gaussian extension see [14]. The present abundance of DM in the form of PBHs per logarithmic mass interval $d \ln M$ is given by

$$f_{\text{PBH}}(M) \equiv \frac{1}{\rho_{\text{DM}}} \frac{d\rho_{\text{PBH}}}{d \ln M} \simeq \left(\frac{\beta_M}{7 \cdot 10^{-9}} \right) \left(\frac{\gamma}{0.2} \right)^{1/2} \left(\frac{106.75}{g_*} \right)^{1/4} \left(\frac{M_{\odot}}{M} \right)^{1/2}, \quad (1.7)$$

where $\gamma < 1$ is a parameters introduced to take into account the efficiency of the collapse.

A peculiar feature of such models is that, after being generated during the last stages of inflation, the sizeable curvature perturbations unavoidably behave as a (second-order) source [15–18] of primordial GWs at horizon re-entry [19]. One can relate the peak frequency of such GWs, close to the characteristic frequency of the corresponding curvature perturbations which collapse to form PBHs, to its mass M by using entropy conservation

$$M \simeq 50 \gamma \left(\frac{10^{-9} \text{ Hz}}{f} \right)^2 M_{\odot}. \quad (1.8)$$

Choosing as frequency the one at which the Laser Interferometer Space Antenna (LISA) project [21] has its maximum sensitivity, i.e. $f_{\text{LISA}} \simeq 3.4$ mHz, Eq. (1.8) gives a mass $M \simeq 10^{-12} M_{\odot}$ (taking $\gamma \simeq 0.2$). Therefore, as also suggested in Ref. [20], LISA measurements can provide useful information on PBH dark matter of such small masses.

As shown in Fig. 1, the fact that the current observational constraints on the PBH abundances of such masses are missing [22], permitting $f_{\text{PBH}} \simeq 1$, is a serendipity. This is possible due to the fact that the Subaru HSC microlensing [23] constraint needs to be cut around the value $10^{-11} M_{\odot}$ under which the geometric optics approximation is not valid for radiation in the optical wavelength [22, 24]. Another constraint analysed in the literature comes from the presence of neutron stars in globular clusters [25], but we do not include it because it is based on controversial assumptions about the dark matter density in these systems. We collect in Appendix A a more detailed discussion of the issues related to these observational constraints.¹

It is certainly an exciting coincidence that the frequency range at which the LISA observatory has its maximum sensitivity corresponds to a region of the mass spectrum where the totality of dark matter composed of PBHs is allowed.

In this paper we demonstrate that, if dark matter is composed by PBHs of masses around $10^{-12} M_{\odot}$, then LISA will be able to measure both the power spectrum of the GWs necessarily generated by the production mechanism of PBHs and their three-point correlator (bispectrum). To do that we study in detail the appropriate and corresponding LISA response functions. Measuring the bispectrum of the GWs is decisive as it will highlight their intrinsic non-Gaussianity, being the source of the GWs at second-order in the primordial curvature perturbation; on the other hand its detection will prove crucial in order to distinguish the origin of the signal between astrophysical origins and primordial ones. Indeed, an astrophysical gravitational wave background is expected to be nearly Gaussian with good approximation since it is formed by the superposition of incoherent sources which cannot be resolved individually.

¹ We briefly comment on the high-mass portion of Fig. 1. The Ultra-Faint Dwarf (UFD) galaxy constraint arises from the fact that PBHs of this mass would cause the dissolution of star clusters observed in UFDs such as Eridanus II [26]; this constraint is strongly weakened in the presence of an intermediate-mass black hole, providing a binding energy that stabilizes the cluster [26, 27]. We thank Juan García-Bellido for discussions on this issue. Secondly, we do not show in Fig. 1 the lensing bounds related to the measured luminosities of Supernovae Ia derived in [28, 29], which constrain the abundance of PBHs above $1 M_{\odot}$.

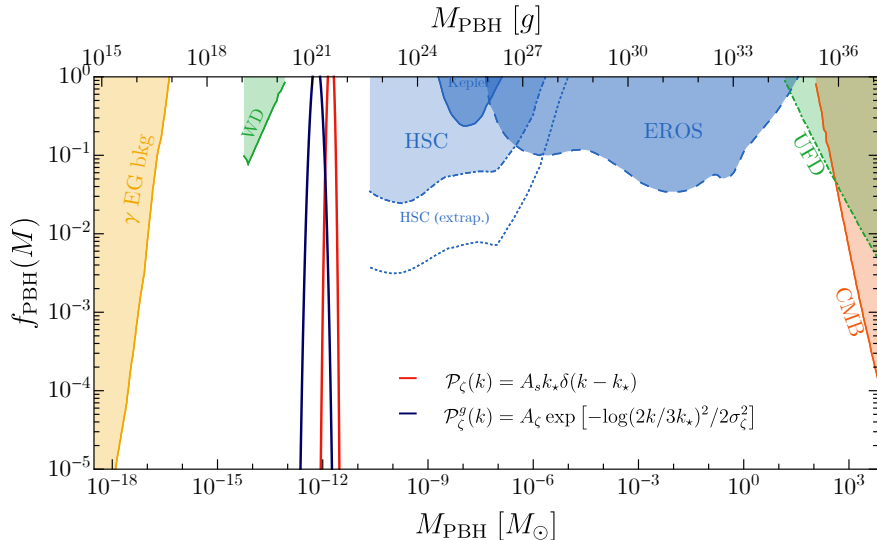


FIG. 1: Overview on the present experimental constraints on the abundance of PBH for a monochromatic spectrum (from Ref. [31] and references therein): in orange, constraints from the CMB; in green, dynamical constraints from White Dwarves and Ultra-Faint Dwarf galaxies; in blue, micro- and milli-lensing observations from Eros, Kepler, Subaru HSC; in yellow, the observations of extra-galactic γ -ray background. Superimposed can be found the PBH abundances as a function of mass obtained for both power spectra in Eqs. (2.13) and (2.15), where we have defined $k_* = 2\pi f_{\text{LISA}}$. The total abundance is obtained by integrating over the masses and the parameters have been chosen to get a PBH abundance equal to the one of dark matter, respectively $A_s = 0.033$, $A_z = 0.044$ and $\sigma_z = 0.5$.

The reader should also be aware of the fact that the PBH abundance is exponentially sensitive to the amplitude of the variance. This means that a small decrease of σ_Δ^2 (and therefore the amplitude of the power spectrum of the comoving curvature perturbation) may reduce significantly the abundance. This, to some extent, plays in our favour as it implies that, even if $f_{\text{PBH}} \ll 1$, the corresponding GWs might be anyway tested by LISA.

The paper is organised as follows. In section II we describe the calculation leading to the GW power spectrum for two different shapes of the comoving curvature perturbations; section III is devoted to the calculation of the GW bispectrum. Section IV contains the details of the response functions leading to the test of non-Gaussianity of the bispectrum discussed in section V. Section VI contains our conclusions. The paper contains as well a couple of Appendices where some technicalities are contained.

A short version of this paper presenting some of the main results can be found in Ref. [30].

II. THE POWER SPECTRUM OF GRAVITATIONAL WAVES

The equation of motion for the GWs is found by expanding the tensor components of the Einstein's equations up to second-order in perturbations

$$h''_{ij} + 2\mathcal{H}h'_{ij} - \nabla^2 h_{ij} = -4\mathcal{T}_{ij}{}^{\ell m} \mathcal{S}_{\ell m}, \quad (2.1)$$

where we defined $'$ to denote the derivative with respect to conformal time η , $d\eta = dt/a$, $\mathcal{H} = a'/a$ as the conformal Hubble parameter as a function of the scale factor $a(\eta)$ and the source term $\mathcal{S}_{\ell m}$ which, in a radiation dominated (RD) universe, takes the form [15]

$$\mathcal{S}_{ij} = 4\Psi\partial_i\partial_j\Psi + 2\partial_i\Psi\partial_j\Psi - \partial_i\left(\frac{\Psi'}{\mathcal{H}} + \Psi\right)\partial_j\left(\frac{\Psi'}{\mathcal{H}} + \Psi\right). \quad (2.2)$$

We note that the mechanism of generation of GWs takes place when the relevant modes re-enter the Hubble horizon; in the case of interest, this happens deep into the radiation-dominated epoch. It is also evident that the source is intrinsically second-order in the scalar perturbation Ψ . For this reason the GWs generated are expected to feature an intrinsic non-Gaussian nature. Additionally, since the source contains two spatial derivatives, the resulting bispectrum in momentum space is expected to peak in the equilateral configuration. The tensor $\mathcal{T}_{ij}{}^{\ell m}$ contracted with the source

term in Eq. (2.1) acts as a projector selecting the transverse and traceless components. Its definition in Fourier space takes the form

$$\tilde{T}_{ij}^{\ell m}(\vec{k}) = e_{ij}^L(\vec{k}) \otimes e^{L\ell m}(\vec{k}) + e_{ij}^R(\vec{k}) \otimes e^{R\ell m}(\vec{k}), \quad (2.3)$$

where $e_{ij}^\lambda(\vec{k})$ are the polarisation tensors written in the chiral basis (L, R).

The scalar perturbation $\Psi(\eta, \vec{k})$ appearing in Eq. (2.2) depends directly on the gauge invariant comoving curvature perturbation through the relation [32]

$$\Psi(\eta, \vec{k}) = \frac{2}{3} T(\eta, k) \zeta(\vec{k}), \quad (2.4)$$

where the transfer function $T(\eta, k)$ in the radiation-dominated era is

$$T(\eta, k) = \mathcal{T}(k\eta), \quad \mathcal{T}(z) = \frac{9}{z^2} \left[\frac{\sin(z/\sqrt{3})}{z/\sqrt{3}} - \cos(z/\sqrt{3}) \right]. \quad (2.5)$$

By defining the dimensionless variables $x = p/k$ and $y = |\vec{k} - \vec{p}|/k$, the solution of the equation of motion (2.1) can be recast in the following form

$$h_{\vec{k}}^\lambda(\eta) = \frac{4}{9} \int \frac{d^3p}{(2\pi)^3} \frac{1}{k^3 \eta} e^\lambda(\vec{k}, \vec{p}) \zeta(\vec{p}) \zeta(\vec{k} - \vec{p}) \left[\mathcal{I}_c(x, y) \cos(k\eta) + \mathcal{I}_s(x, y) \sin(k\eta) \right], \quad (2.6)$$

where we have introduced $e^\lambda(\vec{k}, \vec{p}) = e_{ij}^\lambda(\vec{k}) p^i p^j$ and [35]

$$\begin{aligned} \mathcal{I}_c(x, y) &= 4 \int_1^\infty d\tau \tau (-\sin \tau) \left[2\mathcal{T}(x\tau)\mathcal{T}(y\tau) + \left(\mathcal{T}(x\tau) + x\tau \mathcal{T}'(x\tau) \right) \left(\mathcal{T}(y\tau) + y\tau \mathcal{T}'(y\tau) \right) \right], \\ \mathcal{I}_s(x, y) &= 4 \int_1^\infty d\tau \tau (\cos \tau) \left\{ 2\mathcal{T}(x\tau)\mathcal{T}(y\tau) + \left[\mathcal{T}(x\tau) + x\tau \mathcal{T}'(x\tau) \right] \left[\mathcal{T}(y\tau) + y\tau \mathcal{T}'(y\tau) \right] \right\}. \end{aligned} \quad (2.7)$$

The complete analytical expressions of $\mathcal{I}_c(x, y)$ and $\mathcal{I}_s(x, y)$ can be found in Appendix D of Ref. [35]. We define the power spectrum of GWs using the same primed notation of Eq. (1.3) as

$$\left\langle h^{\lambda_1}(\eta, \vec{k}_1) h^{\lambda_2}(\eta, \vec{k}_2) \right\rangle' \equiv \delta^{\lambda_1 \lambda_2} \frac{2\pi^2}{k_1^3} \mathcal{P}_h(\eta, k_1). \quad (2.8)$$

After having computed the two-point function, in the radiation-dominated era we find $\mathcal{P}_h(\eta, k)$ to be

$$\mathcal{P}_h(\eta, k) = \frac{4}{81} \frac{1}{k^2 \eta^2} \iint_{\mathcal{S}} dx dy \frac{x^2}{y^2} \left[1 - \frac{(1+x^2-y^2)^2}{4x^2} \right]^2 \mathcal{P}_\zeta(kx) \mathcal{P}_\zeta(ky) \left[\cos^2(k\eta) \mathcal{I}_c^2 + \sin^2(k\eta) \mathcal{I}_s^2 + \sin(2k\eta) \mathcal{I}_c \mathcal{I}_s \right], \quad (2.9)$$

where \mathcal{S} is the region in the (x, y) plane allowed by the triangular inequality and shown in Fig. 2 of [35]. The power spectrum of GWs is directly connected to their energy density [35]:

$$\Omega_{\text{GW}}(\eta, k) = \frac{\rho_{\text{GW}}(\eta, k)}{\rho_{\text{cr}}(\eta)} = \frac{1}{24} \left(\frac{k}{\mathcal{H}(\eta)} \right)^2 \overline{\mathcal{P}_h(\eta, k)}, \quad (2.10)$$

where the overline denotes an average over conformal time η . Since the energy density of GWs scales as radiation during the expansion of the universe, we can express its present value as

$$\Omega_{\text{GW}}(\eta_0, k) = \Omega_{r,0} \Omega_{\text{GW}}(\eta_f, k) = \frac{\Omega_{r,0}}{24} \frac{k^2}{\mathcal{H}(\eta_f)^2} \overline{\mathcal{P}_h(\eta_f, k)}, \quad (2.11)$$

where η_f is some time near the end of the radiation-dominated phase and $\Omega_{r,0}$ is the present radiation energy density fraction. The time average of the oscillating terms in Eq. (2.9), together with the simplification of the time factor coming from $\mathcal{H}^2(\eta_f) = 1/\eta_f^2$ (valid in radiation-domination), give the current abundance of GWs

$$\begin{aligned} \Omega_{\text{GW}}(\eta_0, k) &= \frac{\Omega_{r,0}}{72} \int_{-\frac{1}{\sqrt{3}}}^{\frac{1}{\sqrt{3}}} dd \int_{\frac{1}{\sqrt{3}}}^\infty ds \left[\frac{(d^2 - 1/3)(s^2 - 1/3)}{s^2 - d^2} \right]^2 \mathcal{P}_\zeta \left(\frac{k\sqrt{3}}{2}(s+d) \right) \mathcal{P}_\zeta \left(\frac{k\sqrt{3}}{2}(s-d) \right) \\ &\quad \cdot \left[\mathcal{I}_c^2(x(d, s), y(d, s)) + \mathcal{I}_s^2(x(d, s), y(d, s)) \right]. \end{aligned} \quad (2.12)$$

In the last step we also have redefined the integration variables as $d = (x - y)/\sqrt{3}$ and $s = (x + y)/\sqrt{3}$.

A. The case of a Dirac delta power spectrum

In this subsection we make the idealized assumption that the scalar power spectrum has support in a single point

$$\mathcal{P}_\zeta(k) = A_s k_* \delta(k - k_*), \quad (2.13)$$

which can (obviously) be understood as the Gaussian case, discussed in the following subsection, in the limit of very small width. This idealisation has the advantage that it allows to obtain exact analytic results for the amount of GWs produced at second-order by the scalar perturbations. In this subsection we compute the GW abundance, postponing the computation of the bispectrum to the next section.

Inserting Eq. (2.13) in the expression (2.12), the two Dirac delta functions allow to perform the two integrals, and one obtains (see also Refs. [36, 37])

$$\Omega_{\text{GW}}(\eta_0, k) = \frac{1}{15552} \Omega_{r,0} A_s^2 \frac{k^2}{k_*^2} \left(\frac{4k_*^2}{k^2} - 1 \right)^2 \theta(2k_* - k) \left[\mathcal{I}_c^2 \left(\frac{k_*}{k}, \frac{k_*}{k} \right) + \mathcal{I}_s^2 \left(\frac{k_*}{k}, \frac{k_*}{k} \right) \right]. \quad (2.14)$$

This result is shown as a red line in Fig. 2.

B. The case of a Gaussian power spectrum

In this section we generalise the computation of the GWs energy density to the case of a Gaussian-like comoving curvature power spectrum. We take the perturbation, enhanced with respect to the power spectrum on large CMB scales, to be

$$\mathcal{P}_\zeta^g(k) = A_\zeta \exp \left(-\frac{\ln^2(2k/3k_*)}{2\sigma_\zeta^2} \right). \quad (2.15)$$

This case differs from the former due to the wider shape of the power spectrum. From the relation (1.8) we can infer that PBHs of mass $\sim 10^{-12} M_\odot$ can amount for the totality of the dark matter if $\beta_M \sim 6 \cdot 10^{-15}$ (considering $\gamma \sim 0.2$), where we assumed $k_* R_H \simeq 1$ and the threshold to be $\Delta_c \simeq 0.45$. Its rigorous value is determined also by the shape of the power spectrum [13] but, since the most relevant parameter A_ζ is not altered copiously, its impact on GWs is rather small. The corresponding abundance of PBHs is shown by the blue line in Fig. 1, together with the current experimental bounds. We choose $A_\zeta \sim 0.044$ and $\sigma_\zeta = 0.5$. We stress again that a PBH of mass $\sim 10^{-12} M_\odot$ is associated to a scale $k_* \sim k_{\text{LISA}} = 2\pi f_{\text{LISA}} \simeq 2 \cdot 10^{12} \text{Mpc}^{-1}$. The present abundance of GWs is given in Fig. 2 where we see that it falls well within the sensitivity curves of LISA. The different spectral shape with respect to the Dirac delta case is due to the tails of the Gaussian power spectrum of Eq. (2.15). At high frequencies, there is no upper bound at $2k_*$ as in the Dirac delta case, because the scalar power spectrum is non vanishing for $k > k_*$. At lower frequencies, the spectral tilt for the Dirac-delta case is exactly +2 from Eq. (2.13), whereas for the Gaussian case one can show that the tilt is about $\gtrsim 3$ by arguments similar to the ones exposed in Ref. [35].

It is clear that if PBHs of such masses form the totality (or a fraction of) dark matter, LISA will be able to measure the GWs sourced during the PBH formation time.

III. THE BISPECTRUM OF GWS

We already stressed the fact that, being intrinsically at second order, the GWs are non-Gaussian; hence their three-point correlator is not vanishing. One can compute it following the procedure highlighted in Ref. [35]. Computing the three-point function using Eq. (2.6) gives

$$\begin{aligned} \mathcal{B}_{\lambda_i}(\vec{k}_i) &= \left\langle h_{\lambda_1}(\eta_1, \vec{k}_1) h_{\lambda_2}(\eta_2, \vec{k}_2) h_{\lambda_3}(\eta_3, \vec{k}_3) \right\rangle' \\ &= \left(\frac{8\pi}{9} \right)^3 \int d^3 p_1 \frac{1}{k_1^3 k_2^3 k_3^3 \eta_1 \eta_2 \eta_3} \cdot e_{\lambda_1}^*(\vec{k}_1, \vec{p}_1) e_{\lambda_2}^*(\vec{k}_2, \vec{p}_2) e_{\lambda_3}^*(\vec{k}_3, \vec{p}_3) \frac{\mathcal{P}_\zeta(p_1)}{p_1^3} \frac{\mathcal{P}_\zeta(p_2)}{p_2^3} \frac{\mathcal{P}_\zeta(p_3)}{p_3^3} \\ &\quad \cdot \left[\left(\cos(k_1 \eta_1) \mathcal{I}_c \left(\frac{p_1}{k_1}, \frac{p_2}{k_1} \right) + \sin(k_1 \eta_1) \mathcal{I}_s \left(\frac{p_1}{k_1}, \frac{p_2}{k_1} \right) \right) \cdot (1 \rightarrow 2 \text{ and } 2 \rightarrow 3) \cdot (1 \rightarrow 3 \text{ and } 2 \rightarrow 1) \right], \quad (3.1) \end{aligned}$$

where $\vec{p}_2 = \vec{p}_1 - \vec{k}_1$ and $\vec{p}_3 = \vec{p}_1 + \vec{k}_3$.

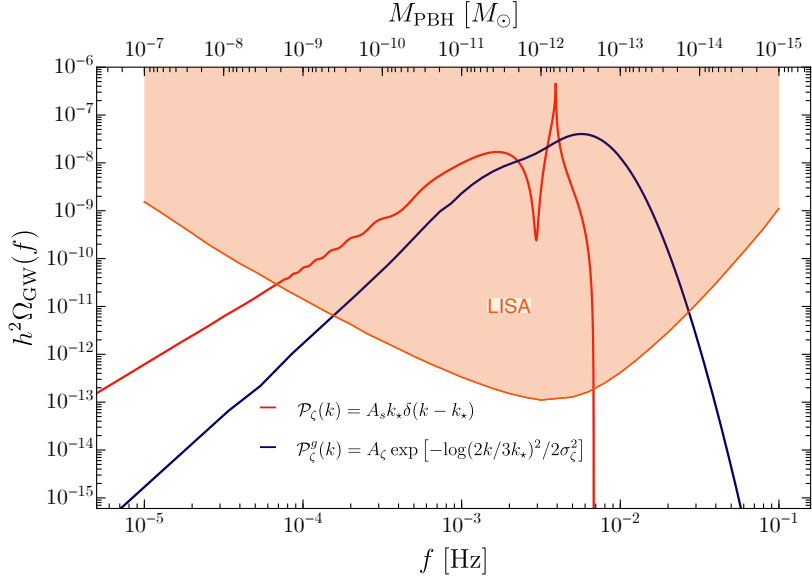


FIG. 2: Comparison of the estimated sensitivity for LISA [33] (the proposed design (4y, 2.5 Gm of length, 6 links) is expected to yield a sensitivity in between the ones dubbed C1 and C2 in Ref. [34]) with the GW abundance generated at second-order by the formation mechanism of PBHs for both power spectra in Eqs. (2.13) and (2.15), where we used the following values for the parameters: $A_s = 0.033$, $A_c = 0.044$ and $\sigma_c = 0.5$.

A. The case of a Dirac delta power spectrum

Inserting Eq. (2.13) into Eq. (3.1), we obtain

$$\begin{aligned} \langle h_{\lambda_1}(\eta_1, \vec{k}_1) h_{\lambda_2}(\eta_2, \vec{k}_2) h_{\lambda_3}(\eta_3, \vec{k}_3) \rangle' &= \left(\frac{8\pi}{9}\right)^3 \frac{A_s^3 k_*^3}{k_1^3 k_2^3 k_3^3 \eta_1 \eta_2 \eta_3} \int d^3 p_1 e_{\lambda_1}^*(\vec{k}_1, \vec{p}_1) e_{\lambda_2}^*(\vec{k}_2, \vec{p}_1 - \vec{k}_1) e_{\lambda_3}^*(\vec{k}_3, \vec{p}_1 + \vec{k}_3) \\ &\cdot \frac{\delta(p_1 - k_*)}{k_*^3} \frac{\delta(|\vec{p}_1 - \vec{k}_1| - k_*)}{k_*^3} \frac{\delta(|\vec{p}_1 + \vec{k}_3| - k_*)}{k_*^3} \prod_{i=1}^3 \left[\cos(k_i \eta_i) \mathcal{I}_c\left(\frac{k_*}{k_i}, \frac{k_*}{k_i}\right) + \sin(k_i \eta_i) \mathcal{I}_s\left(\frac{k_*}{k_i}, \frac{k_*}{k_i}\right) \right]. \end{aligned} \quad (3.2)$$

As studied in Ref. [21], the bispectrum depends on the orientation of the three vectors \vec{k}_i , as well as their magnitude. For definiteness, we fix

$$\vec{k}_1 = k_1 \hat{v}_1, \quad \vec{k}_2 = k_2 \hat{v}_2, \quad \vec{k}_3 = -\vec{k}_1 - \vec{k}_2, \quad (3.3)$$

where

$$\hat{v}_1 = \begin{pmatrix} 1 \\ 0 \\ 0 \end{pmatrix}, \quad \hat{v}_2 = \begin{pmatrix} \frac{k_3^2 - k_1^2 - k_2^2}{2k_1 k_2} \\ \sqrt{1 - \left(\frac{k_3^2 - k_1^2 - k_2^2}{2k_1 k_2}\right)^2} \\ 0 \end{pmatrix}. \quad (3.4)$$

We then use spherical coordinates for the integration vector $\vec{p}_1 = p_1 (\cos \theta, \sin \theta \cos \phi, \sin \theta \sin \phi)$, with $\cos \theta \equiv \xi$. We obtain (exploiting also the orthogonality of the polarization operator e^λ)

$$\begin{aligned} \langle h_{\lambda_1}(\eta_1, \vec{k}_1) h_{\lambda_2}(\eta_2, \vec{k}_2) h_{\lambda_3}(\eta_3, \vec{k}_3) \rangle' &= \left(\frac{8\pi}{9}\right)^3 \frac{A_s^3}{k_*^6 k_1^3 k_2^3 k_3^3 \eta_1 \eta_2 \eta_3} \prod_{i=1}^3 \left[\cos(k_i \eta_i) \mathcal{I}_c\left(\frac{k_*}{k_i}, \frac{k_*}{k_i}\right) + \sin(k_i \eta_i) \mathcal{I}_s\left(\frac{k_*}{k_i}, \frac{k_*}{k_i}\right) \right] \\ &\int_0^\infty dp_1 p_1^2 \int_{-1}^1 d\xi \int_0^{2\pi} d\phi e_{\lambda_1}^*(\vec{k}_1, \vec{p}_1) e_{\lambda_2}^*(\vec{k}_2, \vec{p}_1 - \vec{k}_1) e_{\lambda_3}^*(\vec{k}_3, \vec{p}_1) \delta(p_1 - k_*) \delta\left(\sqrt{k_1^2 + p_1^2 - 2k_1 p_1 \xi} - k_2\right) \\ &\delta\left(\left[k_3^2 + p_1^2 + \frac{(-k_1^2 + k_2^2 - k_3^2) p_1 \xi}{k_1} - \sqrt{2(k_2^2 + k_3^2) - k_1^2 - \frac{(k_2^2 - k_3^2)^2}{k_1^2} p_1 \sqrt{1 - \xi^2} \cos \phi} \right]^{1/2} - k_2\right). \end{aligned} \quad (3.5)$$

A careful study of the Dirac delta functions shows that the integral has support at the two points

$$(\vec{p}_1)_{I,II} = k_1 \left(\frac{1}{2}, \frac{-k_1^2 + k_2^2 + k_3^2}{8\mathcal{A}[k_1, k_2, k_3]}, \pm \frac{\sqrt{16\mathcal{A}^2[k_1, k_2, k_3]k_*^2 - k_1^2 k_2^2 k_3^2}}{4\mathcal{A}[k_1, k_2, k_3]k_1} \right) \equiv k_1 \vec{q}_{I,II}, \quad (3.6)$$

where

$$\mathcal{A}[k_1, k_2, k_3] \equiv \frac{1}{4} \sqrt{(k_1 + k_2 + k_3)(-k_1 + k_2 + k_3)(k_1 - k_2 + k_3)(k_1 + k_2 - k_3)} \quad (3.7)$$

is the area of the triangle of sides k_i . The support is present provided that

$$\mathcal{A}[k_1, k_2, k_3] > \frac{k_1 k_2 k_3}{4k_*}. \quad (3.8)$$

With this in mind, the above integration gives (after some algebra)

$$\begin{aligned} \mathcal{B}_{\lambda_i}(\eta_i, \vec{k}_i) &= \frac{A_s^3 \theta(\mathcal{A}[r_1, r_2, r_3] - \frac{r_1 r_2 r_3}{4})}{k_1^2 k_2^2 k_3^2 k_*^3 \eta_1 \eta_2 \eta_3} \frac{1024\pi^3}{729} \mathcal{D}_{\lambda_i}(\hat{k}_i, r_i) \\ &\quad \cdot \left(\frac{16\mathcal{A}^2[r_1, r_2, r_3]}{r_1^2 r_2^2 r_3^2} - 1 \right)^{-1/2} \frac{r_1^4}{r_2^2 r_3^2} \prod_{i=1}^3 [I_i^* e^{i\eta_i k_i} + I_i e^{-i\eta_i k_i}], \end{aligned} \quad (3.9)$$

where we defined $r_i \equiv k_i/k_*$, and introduced the combinations

$$I_i \equiv \frac{1}{2} \mathcal{I}_c \left(\frac{1}{r_i}, \frac{1}{r_i} \right) + \frac{i}{2} \mathcal{I}_s \left(\frac{1}{r_i}, \frac{1}{r_i} \right), \quad (3.10)$$

as well as the contractions

$$\mathcal{D}_{\lambda_i}(\hat{k}_i, r_i) \equiv e_{ab, \lambda_1}^*(\hat{k}_1) e_{cd, \lambda_2}^*(\hat{k}_2) e_{ef, \lambda_3}^*(\hat{k}_3) \left\{ \left[\vec{q}_a \vec{q}_b (\vec{q} - \hat{k}_1)_c (\vec{q} - \hat{k}_1)_d \vec{q}_e \vec{q}_f \right]_I + [\text{same}]_{II} \right\}, \quad (3.11)$$

where we sum over the two points (3.6). The sum is performed as outlined in Appendix B. We find that the contractions (and, therefore, the full bispectrum) are invariant under parity, namely under the L \leftrightarrow R interchange. The resulting expressions are rather lengthy in the general $r_1 \neq r_2 \neq r_3$ case. In Appendix B we provide the explicit expression for the isosceles case $r_1 = r_2$. In the equilateral case $r_1 = r_2 = r_3$ the equal time bispectrum reads

$$\mathcal{B}_{\lambda_i}^{\text{equil}}(\eta, |\vec{k}_i| = k) = \frac{A_s^3}{k_*^3 \eta^3} \cdot \frac{1}{k^6} \frac{1024\pi^3}{729} \frac{\theta(\sqrt{3}k_* - k)}{\sqrt{\frac{3k_*^2}{k^2} - 1}} \mathcal{I}^3 \left(\frac{k_*}{k} \right) \cdot \begin{cases} \frac{365}{6912} - \frac{61}{192} \frac{k_*^2}{k^2} + \frac{9}{16} \frac{k_*^4}{k^4} - \frac{1}{4} \frac{k_*^6}{k^6} & \text{for RRR, LLL,} \\ \frac{[-4 + (k/k_*)^2]^2 [-12 + 5(k/k_*)^2]}{768(k/k_*)^6} & \text{otherwise.} \end{cases} \quad (3.12)$$

where we have averaged over the oscillations of the amplitude (as done for the power spectrum in [12]), which amounts in the replacement

$$\mathcal{I}_c \left(\frac{1}{r_i}, \frac{1}{r_i} \right) \cos(\eta_i k_i) + \mathcal{I}_s \left(\frac{1}{r_i}, \frac{1}{r_i} \right) \sin(\eta_i k_i) \rightarrow \sqrt{\mathcal{I}_c^2 \left(\frac{1}{r_i}, \frac{1}{r_i} \right) + \mathcal{I}_s^2 \left(\frac{1}{r_i}, \frac{1}{r_i} \right)} \equiv \mathcal{I} \left(\frac{k_*}{k_i} \right) = 2|I_i|. \quad (3.13)$$

In Fig. 3 we show the equilateral (left panel) and isosceles bispectrum generated by the Dirac scalar power spectrum. We see that the bispectrum is peaked in the equilateral configurations, at $k = 2k_*/\sqrt{3}$ (where the function I formally has a logarithmic divergence). This is clear also by looking at the plot of the shape, as defined in Eq. (3.14), shown in Fig. 5 (left). As we discuss in the next section, this peak dominates the signal of the bispectrum at LISA.

B. The case of a Gaussian power spectrum

It is now interesting to analyse the bispectrum corresponding to the Gaussian-like curvature perturbation power spectrum in Eq. (2.15). First, we can compute it in the equilateral configuration, where we set $k_1 = k_2 = k_3$; the result is shown in the left panel of Fig. 4. A few comments can be made at this point. First, we see that the wider

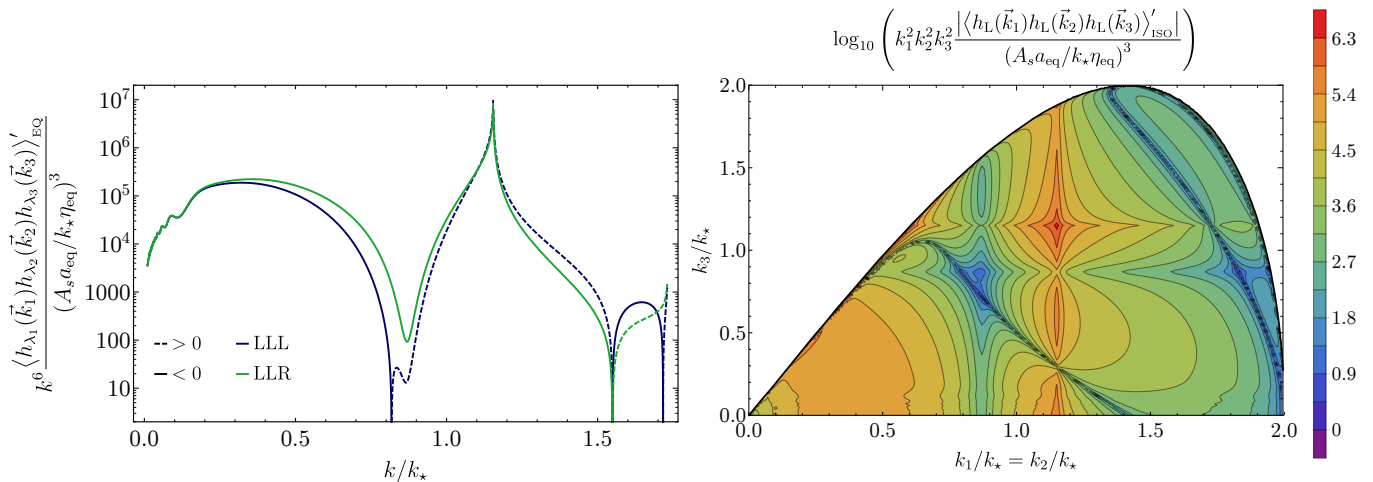


FIG. 3: **Dirac delta power spectrum.** *Left:* Plot of the rescaled bispectrum in the equilateral configuration. The bispectrum vanishes in the outmost right part of the plot, namely for $k > \sqrt{3}k_*$. *Right:* Contour plot of the rescaled bispectrum for the isosceles case. The bispectrum vanishes in the white region.

shape of the power spectrum compared to the Dirac delta one results in a lower peak in the equilateral configuration, making the two peaks with opposite sign in the LLL configuration comparable. Moreover, the width increase causes the bispectrum to be peaked at lower values of the momenta compared to k_* . One has to keep in mind that, for sake of generality, in this case we assumed a power spectrum centred at a different momentum, namely $\sim 3k_*/2$. As we shall see this change of the pivot scale, even though it does not introduce radical changes for what concern the PBH and the GWs abundances, can decrease the significance of the detection at LISA. Finally, we note that the polarization configurations LLR=RRL (and their permutations) are suppressed with respect to the LLL=RRR ones.

In the right panel of Fig. 4 one can see the behaviour of the rescaled three-point function of GWs in the isosceles configuration ($k_1 = k_2$). Two important differences with respect to the Dirac case are its more regular profile and the absence of a cut-off present in the former case due to the Heaviside θ -function.

C. The shape of the bispectrum

We may define the shape for the bispectrum as

$$S_h^{\lambda_1 \lambda_2 \lambda_3}(\vec{k}_1, \vec{k}_2, \vec{k}_3) = k_1^2 k_2^2 k_3^2 \frac{\langle h_{\lambda_1}(\eta, \vec{k}_1) h_{\lambda_2}(\eta, \vec{k}_2) h_{\lambda_3}(\eta, \vec{k}_3) \rangle'}{\sqrt{\mathcal{P}_h(\eta, k_1) \mathcal{P}_h(\eta, k_2) \mathcal{P}_h(\eta, k_3)}}. \quad (3.14)$$

The shape, as defined in Eq. (3.14), is shown in Fig. 5 (right). Our findings show that the bispectrum of GWs has its maximum at the equilateral configuration, $k_1 \simeq k_2 \simeq k_3$. This comes about because the source of the GWs is composed by gradients of the curvature perturbations when the latter re-enters the horizon. The measurement of this shape would by itself provide a consistency relation between the bispectrum and the power spectrum of GWs, which might help disentangling the signal from other possible sources.

IV. LISA RESPONSE FUNCTION FOR THE BISPECTRUM

The LISA constellation consists of three satellites placed at the vertices of an equilateral triangle of side $L = 2.5 \cdot 10^6$ km (the actual distance slightly varies during the orbit; this effect is disregarded in our computations). Laser light is sent from each satellite to the other two, so that each vertex acts as a time delay interferometer. The three measurements are not noise-orthogonal, as any two interferometers share one arm. The noise covariance matrix can however be diagonalized to provide noise-orthogonal combinations. We consider the three linear combinations A,E,T introduced in Ref. [39]. These combinations are also signal-orthogonal; moreover, in the case of equal arms the combination T is insensitive to the signal, and it is often denoted as the null channel. We denote as Σ_O the signal (measurement minus

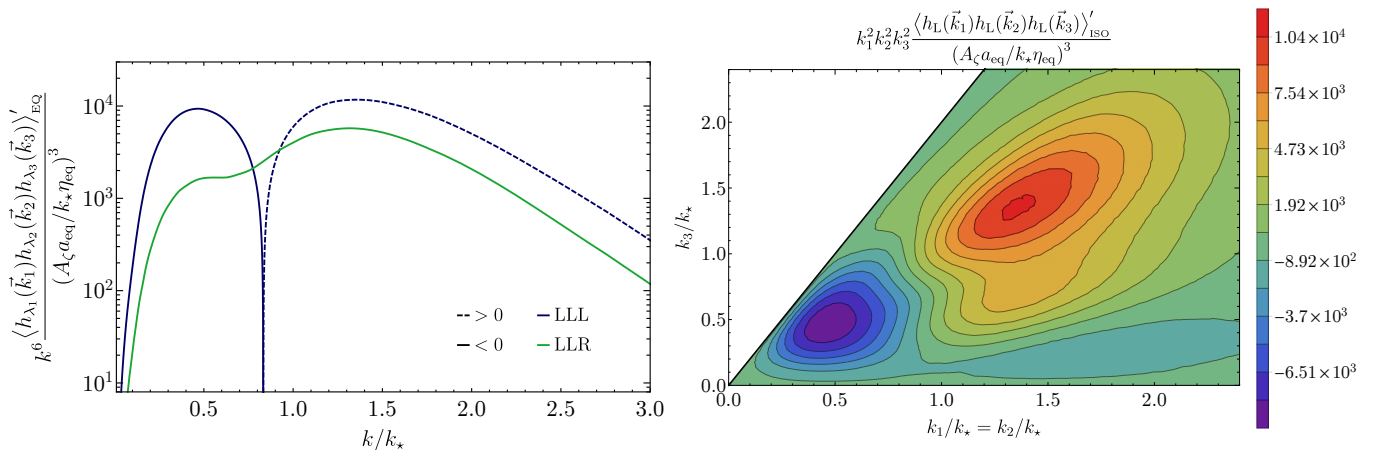


FIG. 4: **Gaussian power spectrum.** *Left:* Plot of the rescaled bispectrum in the equilateral configuration. *Right:* Contour plot of the rescaled bispectrum for the isosceles case. The white region is not allowed due to the triangular inequality imposed on k_1 , k_2 and k_3 by conservation of momentum.

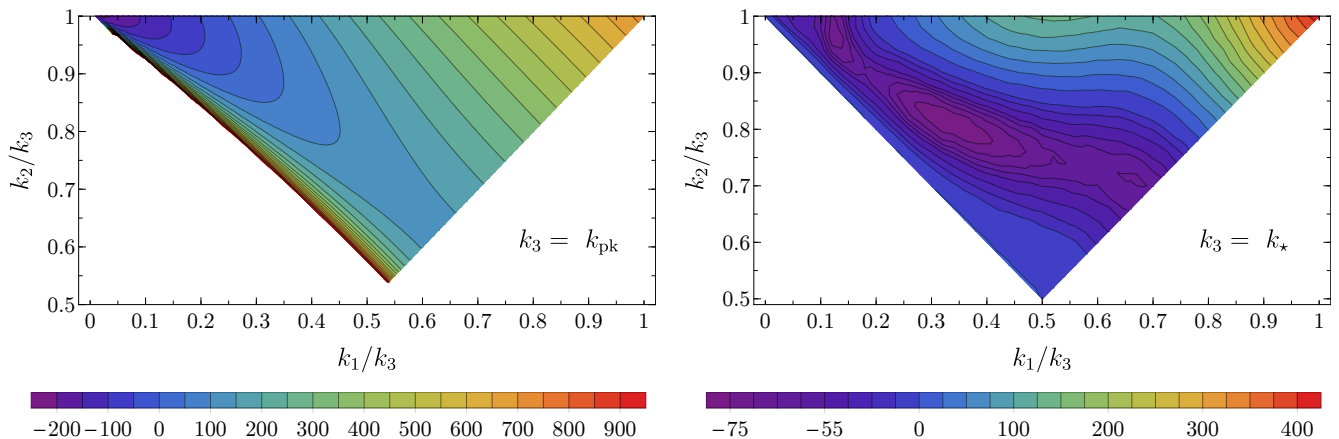


FIG. 5: Shape of the three-point function. *Left:* Dirac delta case. *Right:* Gaussian case.

noise) in the O channel (where O is either A or E). The expectation value for the three-point function of the signal can formally be written as [38]

$$\langle \Sigma_O \Sigma_{O'} \Sigma_{O''} \rangle = \sum_{\lambda_1, \lambda_2, \lambda_3} \int d f_1 d f_2 d f_3 f_1 f_2 f_3 \mathcal{B}_{\lambda_1 \lambda_2 \lambda_3}(\vec{f}_1, \vec{f}_2, \vec{f}_3) \mathcal{R}_{\lambda_1 \lambda_2 \lambda_3}^{O O' O''}(\vec{f}_1, \vec{f}_2, \vec{f}_3). \quad (4.1)$$

In this expression, λ_i and \vec{f}_i denote, respectively, the polarization and frequency (more precisely, the frequency vector, related to the wave vector by $\vec{f} = \vec{k}/2\pi$) of the GWs involved in the correlator; $\mathcal{B}_{\lambda_i}(\vec{f}_i)$ is the GW bispectrum, and \mathcal{R} the three-point response function. As the measurement is a time delay, Σ_O has the dimension of an inverse mass. The bispectrum has mass dimension -6 . With these conventions, the response function is therefore dimensionless. Due to the planar nature of the instrument [40], the response function is invariant under parity, namely $\mathcal{R}_{\text{RRR}} = \mathcal{R}_{\text{LLL}}$, $\mathcal{R}_{\text{RRL}} = \mathcal{R}_{\text{LLR}}$ (and so on). Moreover, due to the highly symmetric configuration, only the EEE and AAE (and permutations) correlations of the channels are nonvanishing, and they are one the opposite of the other $\mathcal{R}^{\text{EEE}} = -\mathcal{R}^{\text{AAE}}$ [38].

All the relevant formulae for the computation of \mathcal{R} can be found in Section 3 of [38], so we do not copy them here. In Figure 6 we show the two response functions $\mathcal{R}_{\text{LLL}}^{\text{EEE}}$ (red line) and $\mathcal{R}_{\text{LLR}}^{\text{EEE}}$ (green line) in the equilateral case $f_1 = f_2 = f_3$. We note that the instrument is significantly more sensitive to equal-helicity bispectrum LLL (and, equivalently, RRR). Moreover, we see that in the outmost left range shown in Figure 6 (left panel), the response

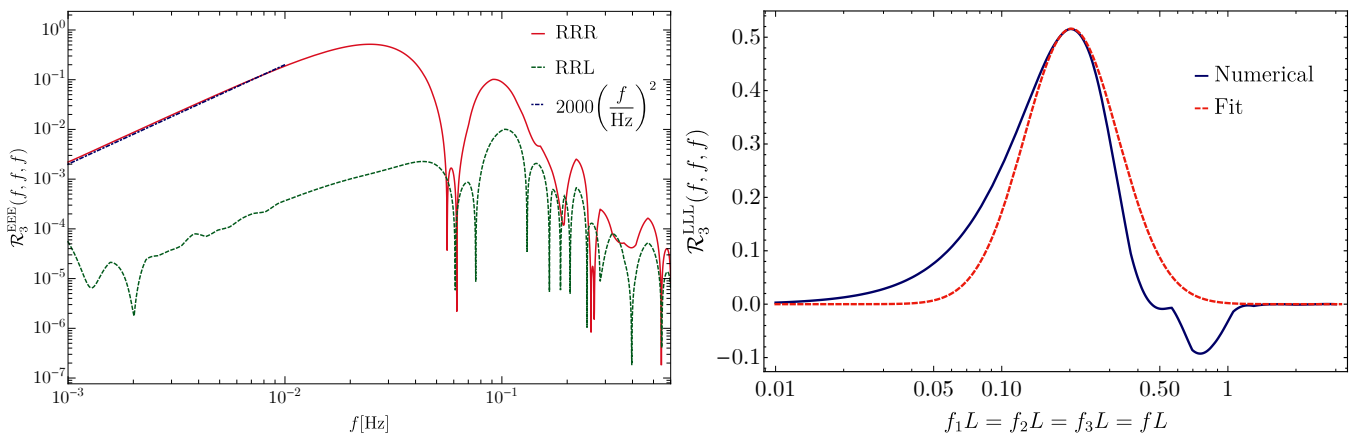


FIG. 6: **Equilateral configuration.** *Left:* Response function $\mathcal{R}_3^{\text{EEE}}(f, f, f)$ for RRR=LLL (red curve) and RRL=LLR (green curve), as a function of the frequency. At $f = 0.002$ Hz the response function in the RRR case is about 500 times greater than in the RRL case. The blue dotted line indicates the expansion at small frequencies of Eq. (4.2). *Right:* Comparison between the response function on equilateral triangles and its 1d fit, see Eq. (4.3).

function can be very well approximated by

$$\mathcal{R}_{\text{LLL}}^{\text{EEE}}(|f_i|) \simeq 2000 \left(\frac{f}{\text{Hz}} \right)^2, \quad 10^{-4} \lesssim \frac{f}{\text{Hz}} \lesssim 10^{-2}. \quad (4.2)$$

It is also useful to approximate the response function at its greatest peak. As shown in the right panel of Figure 6, the peak is well fitted by

$$\mathcal{R}_{\text{RRR}}^{\text{EEE,pk}}(f, f, f) \simeq \left[A e^{-\frac{\ln^2 \frac{f}{f_r}}{2\sigma^2}} \right] \equiv [\mathcal{R}_{\text{fit-1d}}(f)]^3, \quad (4.3)$$

with (matching the peak position, amplitude, and curvature)

$$A \simeq 0.802, \quad f_r \simeq \frac{0.203}{L} \simeq 0.0243 \text{ Hz}, \quad \sigma^2 = 0.686. \quad (4.4)$$

In Ref. [38] only the equilateral $f_1 = f_2 = f_3$ and squeezed isosceles $f_1 = f_2 \gg f_3$ configurations were computed. Here, we compute and study the generic isosceles configuration $f_1 = f_2 \neq f_3$.

As we see in Fig. 7 the response function is peaked in the equilateral configuration, at $f_1 = f_2 = f_3 = f_r$. A significant result is also found in the squeezed limit $f_3 \ll f_1 = f_2 \simeq f_r$. The fitting formula (4.3) can be used to provide a fit of the generic shape next to the peak

$$\mathcal{R}_{\text{RRR}}^{\text{EEE,pk}}(f_1, f_2, f_3) \simeq \bar{A}(f_1, f_2, f_3) \cdot \mathcal{R}_{\text{fit-1d}}(f_1) \mathcal{R}_{\text{fit-1d}}(f_2) \mathcal{R}_{\text{fit-1d}}(f_3), \quad (4.5)$$

where

$$\bar{A}(f_1, f_2, f_3) \equiv \frac{\sqrt{(f_1 + f_2 + f_3)(-f_1 + f_2 + f_3)(f_1 - f_2 + f_3)(f_1 + f_2 - f_3)}}{\sqrt{3}(f_1 f_2 f_3)^{2/3}} \quad (4.6)$$

is the ratio between the area of a triangle of sides f_1, f_2, f_3 , divided by the area of an equilateral triangle of sides $(f_1 f_2 f_3)^{1/3}$. This factor evaluates to one at the peak, and it suppresses the bispectrum at its boundaries, so that the fitting formula (4.3) can be integrated over all possible shapes. In the right panel of the Fig. 7 the fitting function (4.3) is compared against the exact bispectrum for isosceles shapes.

In the next section, the response function is used to elaborate a test of the bispectrum associated with its measurement at LISA (this computation can be easily extended to different instruments). The formulae require integrating over different shapes. This will not be needed in our case, since the bispectrum is highly peaked, so that one can simply evaluate the response function at the peak of the bispectrum.

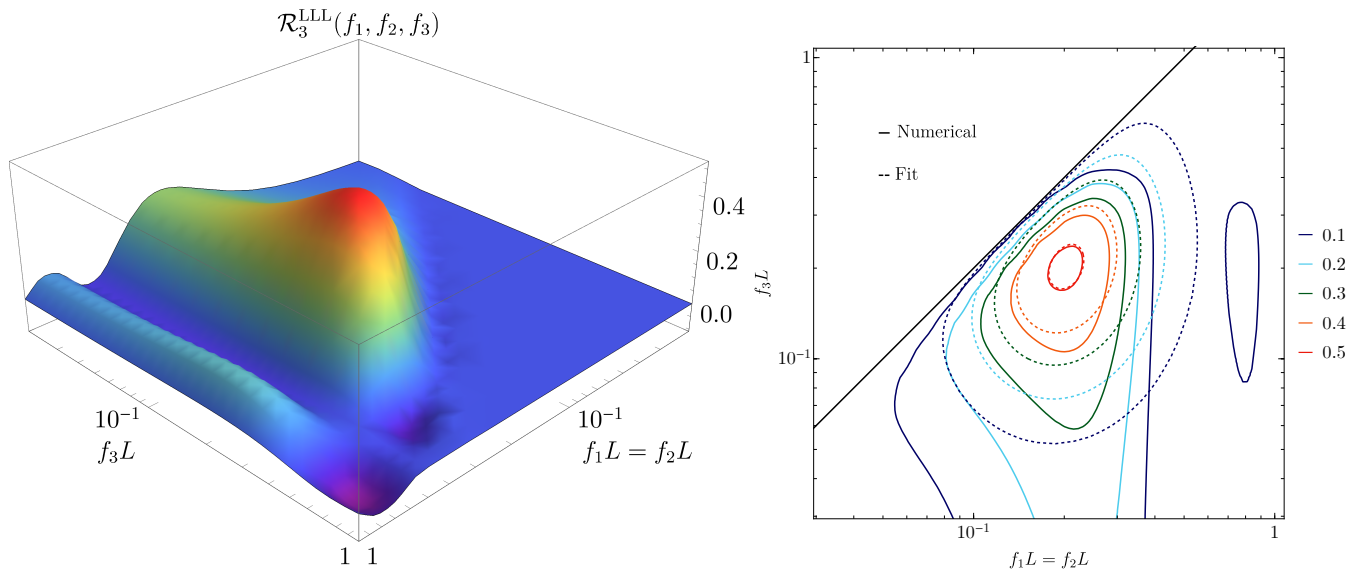


FIG. 7: **Isosceles configuration.** *Left:* 3d plot of the response function $\mathcal{R}_3^{\text{LLL}}(f_1, f_2, f_3)$ in the isosceles configuration. *Right:* Contour plot of $\mathcal{R}_{\text{RRR}}^{\text{EEE}}(f_1, f_2, f_3)$ for EEE and for RRR. We verified that the response function for AAE (and EAA) is the opposite to the one shown here. The black solid line corresponds to the $f_3 = 2f_1$ folded case (notice that the axes are in log units), and the upper-left corner does not exist (it violates the triangular inequality). The bottom part of the region corresponds to squeezed configurations. The dashed lines correspond to the 3d fit for the response function on isosceles triangles (4.5).

V. DETECTING THE BISPECTRUM AT LISA

In this Section we construct an estimator to verify the deviation from Gaussianity of the stochastic GW background obtained from the mechanism we are discussing and measured by LISA. We divide the discussion in two parts. In the first subsection we compute the Fourier transform of the signal measured at LISA. In the second subsection we construct and evaluate the estimator. The computations are performed both for a GW background produced in the idealized case of a delta-function scalar power spectrum, given by Eq. (2.13), and then for the more realistic case of a peaked scalar distribution of finite width, Eq. (2.15).

A. Fourier transform of the signal measured at LISA

The unequal time bispectrum is formally of the type

$$\mathcal{B}_{\lambda_i}(\eta_i, \vec{f}_i) = \mathcal{N} \prod_{i=1}^3 [I_i^* e^{2\pi i f_i \eta_i} + I_i e^{-2\pi i f_i \eta_i}], \quad (5.1)$$

where we have changed from the wavevectors \vec{k}_i to the frequency “vectors” $\vec{f}_i = \vec{k}_i/2\pi$. Combining Eqs. (3.9) (which is the GW bispectrum of modes inside the horizon during the cosmological epoch of radiation domination) with the discussion of Appendix C, one finds, in the case of a Dirac δ power spectrum of the sourcing scalar perturbations²,

$$\mathcal{N} = [\pi \cdot 10^{-20} \text{Hz}]^3 \frac{A_s^3 \theta \left(\mathcal{A}[r_1, r_2, r_3] - \frac{r_1 r_2 r_3}{4} \right)}{(2\pi)^9 f_1^2 f_2^2 f_3^2 f_*^3} \frac{1024\pi^3}{729} \mathcal{D}_{\lambda_i}(\hat{f}_i, r_i) \left(\frac{16 \mathcal{A}^2[r_1, r_2, r_3]}{r_1^2 r_2^2 r_3^2} - 1 \right)^{-1/2} \frac{r_1^4}{r_2^2 r_3^2}. \quad (5.2)$$

The first step to study the significance of the measurement of the bispectrum at LISA is to perform the Fourier transform of the three time variables η_i appearing in Eq. (5.1). We first need to compute the Fourier transform of the

² The relation (5.2) is used in the final step leading to Eq. (5.20). The computations performed here until Eq. (5.20) are based on the more general expression (5.1).

unequal-time GW bispectrum. The times η_i of the three measurements can be decomposed as a common cosmological time η_{cosm} plus two time differences between the measurements. Therefore

$$\eta_1 - \eta_2 \equiv \Delta_2, \quad \eta_1 - \eta_3 \equiv \Delta_3, \quad \eta_1 + \eta_2 + \eta_3 \equiv 3\eta_{\text{cosm}}. \quad (5.3)$$

Only the time differences are relevant for the computation. Physically, the experimental output taken in the 4–10 years of operation cannot depend on the age of the universe (apart from the cosmological rescaling of the GW amplitude that has already been taken into account in Eq. (5.1)). Mathematically, phases proportional to η_{cosm} in the Fourier transform are fast oscillating, and average to zero. For this reason, we simply set $\eta_{\text{cosm}} = 0$ in the phases of eq. (5.1), so that

$$\mathcal{B}_{\lambda_i}(\eta_i, \vec{f}_i) \cong \mathcal{N} \left[I_1^* e^{i\frac{2\pi}{3}f_1(\Delta_2+\Delta_3)} + \text{c.c.} \right] \left[I_2^* e^{i\frac{2\pi}{3}f_2(\Delta_3-2\Delta_2)} + \text{c.c.} \right] \left[I_3^* e^{i\frac{2\pi}{3}f_3(\Delta_2-2\Delta_3)} + \text{c.c.} \right]. \quad (5.4)$$

where c.c. denotes complex conjugation. The Fourier transform of this expression reads

$$\begin{aligned} \tilde{\mathcal{B}}_{\lambda_i}(F_i, f_i, \hat{f}_i) &\equiv \int d\eta_1 d\eta_2 d\eta_3 e^{-2\pi i(F_1\eta_1 + F_2\eta_2 + F_3\eta_3)} \mathcal{B}_{\lambda_i}(\eta_i, \vec{f}_i) \\ &= \delta(F_1 + F_2 + F_3) \int d\Delta_2 \int d\Delta_3 e^{2\pi i[F_2\Delta_2 + F_3\Delta_3]} \mathcal{B}_{\lambda_i}(\Delta_2, \Delta_3, \vec{f}_i), \end{aligned} \quad (5.5)$$

where the emergence of the overall Dirac delta is due to the fact that (5.4) only depends on the difference between the times. This expresses the statistical time invariance of the bispectrum, when measured over times much smaller than the cosmological time. As we will see, this ensures that the ratio that we compute in the next subsection grows as the square root of the time T over which the measurement is taken.

From the Fourier transform of the bispectrum we can compute the expectation value for the three-point function of the signal (in frequency space) measured in the O_i LISA output channels [38]

$$\begin{aligned} \langle \tilde{\Sigma}_{O_1}(F_1) \tilde{\Sigma}_{O_2}(F_2) \tilde{\Sigma}_{O_3}(F_3) \rangle &= \delta(F_1 + F_2 + F_3) L^3 \int d\ln f_1 \int d\ln f_2 \int d\ln f_3 f_1^2 f_2^2 f_3^2 \tilde{\mathcal{B}}_{\lambda_i}(F_i, f_i, \hat{f}_i) \mathcal{R}_{\lambda_1\lambda_2\lambda_3}^{O_1O_2O_3}(\vec{f}_1, \vec{f}_2, \vec{f}_3) \\ &\equiv \delta(F_1 + F_2 + F_3) S_s^{O_1O_2O_3}(F_1, F_2, F_3). \end{aligned} \quad (5.6)$$

With a completely analogous computation, the expectation value of the two-point function of the unequal time signal is (in frequency space)

$$\langle \tilde{\Sigma}_{O_1}(F_1) \tilde{\Sigma}_{O_2}(F_2) \rangle = \delta(F_1 + F_2) \delta_{O_1O_2} \cdot \frac{L^2}{2|F_1|} \sum_{\lambda} P_{\lambda}(|F_1|) \mathcal{R}_{O_1O_1,\lambda}(|F_1|), \quad (5.7)$$

where $\mathcal{R}_{OO,\lambda}$ is the two-point response function (see, e.g., [39] and the discussion in [38]).

B. Test of non-Gaussianity

We are now in position to construct the estimator

$$\hat{\mathcal{F}} \equiv \sum_{ijk} \int dF_1 dF_2 dF_3 W^{ijk}(F_1, F_2, F_3) \tilde{s}_i(F_1) \tilde{s}_j(F_2) \tilde{s}_k(F_3), \quad (5.8)$$

where \tilde{s} is the Fourier transform of the measurement, given by the sum of the GW-induced signal $\tilde{\Sigma}$ plus noise \tilde{n} . The noise is assumed to be Gaussian³ and uncorrelated to the signal. The LISA output channels are constructed so to be noise-orthogonal [39], and the power spectrum in the A and E channels reads

$$\langle n_i(F_1) n_j(F_2) \rangle = \delta_{ij} (2L)^2 P_n(|F_1|) \delta(F_1 + F_2), \quad \{i, j\} = \{A, E\}, \quad (5.9)$$

³ As discussed in Ref. [38], this is the case for a large range of frequencies centered around 1 mHz in the LISA Pathfinder mission. Moreover, this is taken as a working assumption in the LISA Data Challenge.

where $P_n(F)$ has the dimension of time and can be found for instance in Ref. [44]. Eqs. (5.7) and (5.9) add up to give the power associated to the measurement $s_i = \Sigma_i + n_i$:

$$P_s(|F|) \equiv 4L^2 P_n(|F|) + \frac{L^2}{|F|} P_R(|F|) \mathcal{R}_{EE,R}(|F|), \quad (5.10)$$

where we have performed the sum over the two GW helicities appearing in Eq. (5.7), using the fact that they have identical power, $P_L = P_R$, and the fact that the detector response function satisfies $\mathcal{R}_{AA,L} = \mathcal{R}_{AA,R} = \mathcal{R}_{EE,L} = \mathcal{R}_{EE,R}$.

The estimator for testing the presence of non-Gaussianity is a linear combination (sum over the LISA output channels i, j, k , and over the frequencies F_i) of the LISA measurement, with the coefficients $W^{ijk}(F_1, F_2, F_3)$ chosen so to maximize the ratio

$$\text{TNG} \equiv \frac{\langle \hat{\mathcal{F}} \rangle}{\langle \hat{\mathcal{F}}^2 \rangle_{\text{PS}}^{1/2}}, \quad (5.11)$$

where the suffix _{PS} indicates that only the contributions from the two-point function of the measurement are included in the denominator. If the underlying statistics is Gaussian, the measurement of (5.11) is expected to be a order one quantity. We emphasize that, strictly speaking, this ratio is not the standard signal-to-noise ratio, since the denominator in Eq. (5.11) does not contain the full variance of $\hat{\mathcal{F}}$. Our choice is justified by the fact that, as shown in Refs. [45, 46], the quantity (5.11) obeys approximately a χ^2 -statistic with a non-vanishing non-centrality parameter [45] that is non-vanishing if the stochastic GW is non-Gaussian. In this sense, we dubbed this ratio as Test of Non-Gaussianity (TNG), since obtaining a large value for this ratio clearly indicates the presence of a strong non-Gaussianity. We will elaborate further on this point in Ref. [47].

Under the assumption of Gaussian noise, only the signal contributes to the expectation value at the numerator,

$$\langle \hat{\mathcal{F}} \rangle = \sum_{ijk} \int dF_1 dF_2 dF_3 W^{ijk}(F_1, F_2, F_3) \delta(F_1 + F_2 + F_3) S_s^{ijk}(F_1, F_2, F_3), \quad (5.12)$$

where Eq. (5.6) has been used. For the denominator, instead, Eqs. (5.7) and (5.9) lead to

$$\begin{aligned} \langle \hat{\mathcal{F}}^2 \rangle_{\text{PS}} &= \sum_{ijk} \int dF_1 dF_2 dF_3 P_s(|F_1|) P_s(|F_2|) P_s(|F_3|) \\ &\cdot [6 W^{ijk}(F_1, F_2, F_3) W^{ijk}(F_1, F_2, F_3)^* + 9 W^{ijj}(F_1, F_2, -F_2) W^{ikk}(F_1, F_3, -F_3)^*], \end{aligned} \quad (5.13)$$

Using the fact that P_n is extremely large at $F \rightarrow 0$, one can show [38] that the ratio (5.11) is maximized by the choice

$$W^{ijk}(F_1, F_2, F_3) \propto \delta(F_1 + F_2 + F_3) \frac{S_s^{ijk}(F_1, F_2, F_3)}{P_s(|F_1|) P_s(|F_2|) P_s(|F_3|)}, \quad (5.14)$$

which, once inserted into Eqs. (5.12) and (5.11), leads to

$$\text{TNG} = \left[\frac{T}{6} \sum_{ijk} \int dF_1 dF_2 dF_3 \delta(F_1 + F_2 + F_3) \frac{S_s^{ijk}(F_1, F_2, F_3)}{P_s(|F_1|) P_s(|F_2|) P_s(|F_3|)} \right]^{1/2}, \quad (5.15)$$

where T is the observation time (the nominal duration of the LISA mission is 4 years, with a 75% duty cycle. However, the mission will be designed to last for ~ 10 years [33]).

This expression is denoted as the signal-to-noise ratio for the measurement of the bispectrum in Ref. [38]. To be precise, Ref. [38] only included the power spectrum of the noise at the denominator of this expression, under the assumption of weak signal ($P_s \ll P_n$). At the mathematical level, their computation can be immediately extended to the present one, by replacing P_n with the sum (5.10), as we have just done. Physically, we see from Fig. 2 that the weak signal assumption does not hold in our case, and (although this should be checked model by model) it is questionable whether it applies to the situations in which the signal is large enough to give a visible three-point correlation. The proper inclusion done here clearly results in a decrease of (5.15) with respect to the case in which only P_n is included at the denominator.

Let us now proceed with the evaluation of Eq. (5.15). We insert the expression (5.4) into (5.5), and rewrite the integral as a sum of terms which contain one phase each. For each term, the integration of these phases over the times Δ_2, Δ_3 results into two Dirac delta functions (this assumes a total integration time much greater than the frequencies

of our interest, which is clearly the case). The two Dirac delta functions are used to eliminate the integrals over f_2 and f_3 appearing in Eq. (5.6). In this way, these two variables are replaced by linear combinations containing f_1, F_2, F_3 (we note that F_1 can be substituted by $-F_2 - F_3$, due to the overall $\delta(F_1 + F_2 + F_3)$). In the replacement we need to account for constraints arising from the fact that the variables f_i in Eq. (5.6) are non-negative (being the magnitudes of \vec{f}_i), while the frequencies F_i in the Fourier decomposition of the signal can have either signs. These constraints are enforced by θ -functions. Keeping all this into account, we obtain,

$$\begin{aligned} \text{TNG} = & \left\{ \frac{2T}{3} \int_{-\infty}^{+\infty} dF_2 \int_{-\infty}^{+\infty} dF_3 \frac{81L^6}{P_s(|F_2 + F_3|) P_s(|F_2|) P_s(|F_3|)} \right. \\ & \cdot \left| \int_{-\infty}^{\infty} df_1 |f_1| |f_1 + 2F_2 + F_3| |f_1 + F_2 + 2F_3| \left\{ \theta(f_1) I^* \left[\frac{f_\star}{|f_1|} \right] + \theta(-f_1) I \left[\frac{f_\star}{|f_1|} \right] \right\} \right. \\ & \left. \left\{ \theta(f_1 + 2F_2 + F_3) I^* \left[\frac{f_\star}{|f_1 + 2F_2 + F_3|} \right] + \theta(-f_1 - 2F_2 - F_3) I \left[\frac{f_\star}{|f_1 + 2F_2 + F_3|} \right] \right\} \right. \\ & \left. \left\{ \theta(f_1 + F_2 + 2F_3) I^* \left[\frac{f_\star}{|f_1 + F_2 + 2F_3|} \right] + \theta(-f_1 - F_2 - 2F_3) I \left[\frac{f_\star}{|f_1 + F_2 + 2F_3|} \right] \right\} \right. \\ & \left. \cdot \sum_{\lambda_i} \mathcal{N}_{\lambda_i}(|f_1|, |f_1 + 2F_2 + F_3|, |f_1 + F_2 + 2F_3|) \mathcal{R}_{\lambda_i}^{\text{EEE}}(|f_1|, |f_1 + 2F_2 + F_3|, |f_1 + F_2 + 2F_3|) \right| \Bigg\}^{1/2}, \end{aligned} \quad (5.16)$$

where, for clarity, we have written down explicitly the helicities and the frequencies' dependence of \mathcal{N} , and we have denoted within a square bracket the argument on which I depends on.⁴ Moreover, we have used the fact that the only nonvanishing three-point response functions are \mathcal{R}^{EEE} and \mathcal{R}^{AAE} (plus permutations), and that they are equal in magnitude. This expression is exact. We rewrite the integral in this expression as

$$\int_{-\infty}^{\infty} dF_2 \int_{-\infty}^{\infty} dF_3 \int_{-\infty}^{\infty} df_1 \int_{-\infty}^{\infty} dg_1 \mathcal{F}(F_2, F_3, f_1) \mathcal{F}^*(F_2, F_3, g_1). \quad (5.17)$$

We can obtain an approximate but still very accurate simpler expression, by exploiting the fact that the integrand $\mathcal{F} \cdot \mathcal{F}^*$ peaks where the arguments of I evaluates to $\frac{\sqrt{3}}{2}$, where

$$\lim_{x \rightarrow \frac{\sqrt{3}}{2}} I(x) = 36 i \ln \left| \frac{2x}{\sqrt{3}} \right|. \quad (5.18)$$

(We notice that this is an integrable singularity, so that (5.16) is finite). The maximum support to the integral occurs where all the functions I contained in the integrand are evaluated at the peak. This occurs only when⁵

$$\begin{aligned} f_1 = g_1 = & \pm \frac{\sqrt{3}}{2} f_\star \quad \text{and} \\ \{F_2, F_3\} = & \left\{ \frac{2f_1}{3}, -\frac{4f_1}{3} \right\} \quad \text{or} \quad \left\{ -\frac{4f_1}{3}, \frac{2f_1}{3} \right\} \quad \text{or} \quad \left\{ -\frac{2f_1}{3}, -\frac{2f_1}{3} \right\} \\ & \text{and} \\ \{F_2, F_3\} = & \left\{ \frac{2g_1}{3}, -\frac{4g_1}{3} \right\} \quad \text{or} \quad \left\{ -\frac{4g_1}{3}, \frac{2g_1}{3} \right\} \quad \text{or} \quad \left\{ -\frac{2g_1}{3}, -\frac{2g_1}{3} \right\} \end{aligned} \quad (5.19)$$

We note that, in particular, this requires $g_1 = f_1$. Based on this, we evaluate the product in Eq. (5.17) under the assumption that $g_1 = f_1$. In this limit, the multiplication between \mathcal{F} and \mathcal{F}^* involves factors of the type $[\theta(x) I^* + \theta(-x) I][\theta(x) I + \theta(-x) I^*] = |I|^2 = \mathcal{I}^2/4$.⁶ In the final expression we still keep f_1 and g_1 as distinct.

⁴ In Eq. (5.16) the range of integration of df_1 runs from $-\infty$ to $+\infty$ as it arises after a sum over two terms, in which f_1 is non-negative (as mentioned above). After sending $f_1 \rightarrow -f_1$ in one of the two terms, the two terms acquire the same formal expression, once expressed in terms of $|f_1|$, and the extrema of integration can therefore be combined as in Eq. (5.16).

⁵ We disregard the $F_2 = F_3 = 0$ case, in which P_n at the denominator of Eq. (5.16) diverges.

⁶ There are three $|I|^2$ combinations in the integrand. This gives rise to the factor $1/64$ in the next expression.

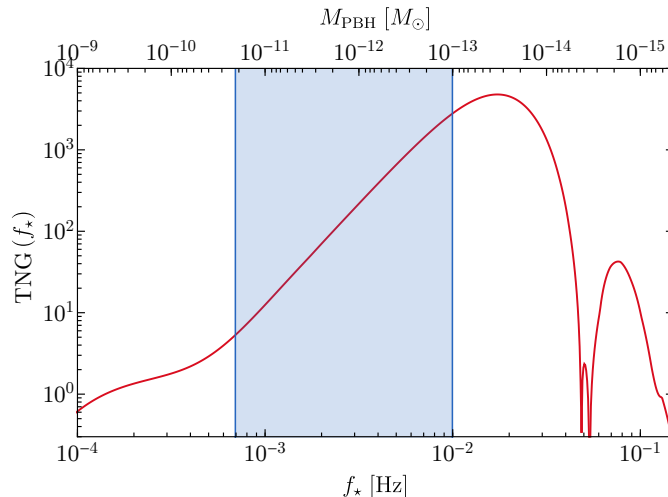


FIG. 8: Expected TNG value obtained from the LISA mission after its nominal duration (4 years with 75% efficiency), for sourcing scalar perturbations with a Dirac delta function power spectrum at the scale f_* , under the assumption that the PBH resulting from this bump are the dark matter of the universe. The blue band in the Figure represents the available window for the PBH-dark matter association.

Clearly, this is just an approximation, rather than an exact evaluation of (5.16), that we perform exploiting the peaked nature of the integrand.

In this way, the θ -functions drop out of Eq. (5.16), and one is left with products of I and \mathcal{N} that precisely form the bispectrum after average over the fast oscillating phases (cf. Eq. (3.13)). Therefore we finally obtain

$$\text{TNG} \simeq \left\{ \frac{2T}{3} \int_{-\infty}^{+\infty} dF_2 \int_{-\infty}^{+\infty} dF_3 \frac{81L^6}{P_s(|F_2 + F_3|) P_s(|F_2|) P_s(|F_3|)} \cdot \frac{1}{64} \left| \int_{-\infty}^{\infty} df_1 |f_1| |f_1 + 2F_2 + F_3| |f_1 + F_2 + 2F_3| \sum_{\lambda_i} \mathcal{B}_{\lambda_i}(|f_1|, |f_1 + 2F_2 + F_3|, |f_1 + F_2 + 2F_3|) \mathcal{R}_{\lambda_i}^{\text{EEE}}(|f_1|, |f_1 + 2F_2 + F_3|, |f_1 + F_2 + 2F_3|) \right|^2 \right\}^{1/2}. \quad (5.20)$$

A direct inspection of the integrand shows that it is highly peaked at the peaks of the bispectrum, given by Eq. (5.19). In this region the response function has a considerably milder dependence on the frequencies, so we can simply evaluate it setting all its arguments to $f_{\text{pk}} = 2/\sqrt{3}f_*$. Moreover, we only include the equal helicity RRR and LLL cases in the sum, due to the strong hierarchy between the equal and unequal helicity response functions (see Figure 6). Both terms give the same contribution, since the response function and the bispectrum are invariant under parity.

We evaluated Eq. (5.20) for $T = 3$ years, and for sourcing scalar perturbations with both a Dirac delta power spectrum and a Gaussian power spectrum. The former choice leads to the numerical values of TNG shown in Figure 8. In the regime of strong signal considered here (cf. Eq. (2)) the power spectrum P_s is highly dominated by the signal part, and it is proportional to the second power of the scalar amplitude A_s . Therefore the dependence on A_s cancels out in the ratio $B_s/P_s^{3/2}$, and the value of TNG is essentially insensitive to A_s ⁷. Therefore, TNG only depends on the value of f_* , as shown in the figure. We see from the figure that the LISA measurement allows to test with high accuracy the non-Gaussianity of the GW background formed in this scenario. It is natural to ask how much the large TNG values shown in the Figure depend on the assumption of a delta power spectrum of the scalar perturbations. For this reason, we also evaluated the expression (5.20) for a Gaussian bump (2.15) of finite width, with an amplitude still chosen so to produce a PBH abundance identical to that of the present dark matter. We vary the central position of the bump, as well as its width. As a measure of the width, we define the ratio $Q \equiv f_{\text{pk},\zeta}/\Delta f$, where we define as Δf the difference between the frequency of the two points (one at the right and one at the left of the peak frequency $f_{\text{pk},\zeta}$) where the scalar power spectrum evaluates to 1/2 times the value at the peak. A large (small) Q -value corresponds

⁷ The noise dominates over the signal at very small and very large frequency, regulating the expression (5.20). These regions give a negligible contribution to the integral, so that, strictly speaking, the value of TNG has a non-vanishing but negligible dependence on A_s .

to a narrow (broad) bump. We performed the computation for three cases:

$$\begin{aligned}
\text{Case 1 : } & f_{\text{pk,bispectrum}} \simeq 0.0058 \text{ Hz} , \quad Q = 4. , \quad \text{TNG} = 50, \\
\text{Case 2 : } & f_{\text{pk,bispectrum}} \simeq 0.0045 \text{ Hz} , \quad Q = 0.8 , \quad \text{TNG} = 2.4, \\
\text{Case 3 : } & f_{\text{pk,bispectrum}} \simeq 0.0017 \text{ Hz} , \quad Q = 0.34 , \quad \text{TNG} = 0.1.
\end{aligned}
\tag{5.21}$$

The progressive decrease of TNG in these results is a combination of two effects: (1) the peak position of the bispectrum is at progressively smaller values (where, as also in the case of a Dirac delta scalar power, the TNG value decreases, due to the decrease of the response function), and (2) the broadening of the bump. The second effect is due to the fact that, for very narrow bumps, the peaks of \mathcal{I} entering at the numerator and at the denominator of (5.20) occur at sufficiently far apart frequencies. As the bump broaden, the peaks at the denominator overlap with those at the numerator, resulting in a decrease of the integrand. The examples show that a large TNG is found for a large portion of parameters compatible with the PBHs as dark matter.

VI. CONCLUSIONS

In this paper we have investigated the capability of the LISA project to detect the non-Gaussian GWs generated during the physical process giving rise to PBHs. The latter are formed through the collapse of the initial large scalar perturbations generated during inflation at the moment when they re-enter the horizon in the radiation-dominated phase. The very same scalar perturbations act as a second-order source for the GWs, which therefore are born non-Gaussian.

If the corresponding PBH masses are in the range around $\sim 10^{-12}M_{\odot}$, not only these PBHs may form the totality of the dark matter, but also the present frequency of the corresponding GWs happens to be in the ballpark of the mHz, precisely where LISA has its maximum sensitivity. We have shown that LISA will detect such signal, both through the two-point correlator and in the three-point correlator. We have done so by studying in detail the LISA response function for the bispectrum, and a corresponding estimator that allows to test the presence of the non-Gaussianity of the GWs.

Furthermore, if a precise measurement of the shape of the non-Gaussianity, with a clear consistency relation with the power spectrum, can be obtained, one would be able to confirm the primordial origin of the stochastic GW background, and also to discriminate between different cosmological models [47].

Finally, the absence of a GW signal will tell us that PBHs of masses around $\sim 10^{-12}M_{\odot}$ are not the dark matter we observe in the universe. As already mentioned in the introduction, however, a detection of a GW signal will be still compatible with our universe populated by such PBH's in smaller abundances.

Note added

While completing this work, Ref. [48] appeared which also noted that PBHs as dark matter with masses around $10^{-12}M_{\odot}$ are associated to GWs which can be detected by LISA. However, there the investigation is limited to the GWs power spectrum, and the study of the bispectrum and its detectability is not present.

Acknowledgments

N.B. acknowledges partial financial support by the ASI/INAF Agreement I/072/09/0 for the Planck LFI Activity of Phase E2. He also acknowledges financial support by ASI Grant 2016-24-H.0. A.R. is supported by the Swiss National Science Foundation (SNSF), project *The Non-Gaussian Universe and Cosmological Symmetries*, project number: 200020-178787. This research was supported in part by Perimeter Institute for Theoretical Physics. Research at Perimeter Institute is supported by the Government of Canada through the Department of Innovation, Science and Economic Development and by the Province of Ontario through the Ministry of Research, Innovation and Science.

Appendix A: Absence of constraints on PBHs as Dark Matter for $10^{-13} - 10^{-11} M_\odot$

In this Appendix we review the reasons why the PBH mass region of interest to our paper, between 10^{-13} and $10^{-11} M_\odot$, is currently unconstrained by observational constraints⁸.

One controversial bound falling in this mass window is the dynamical constraint related to the effect of PBHs on neutron stars in their surroundings. For low masses $M_{\text{PBH}} \sim 10^{-14} - 10^{-13} M_\odot$, PBHs could be dense enough to collide with White Dwarves (WD), compact stars which could be dynamically heated by the passage PBHs and explode as supernovae. The observed WD density prevents PBHs in this mass range from forming all of DM [41]. Neutron Stars (NS) are much smaller and denser than WD, and a PBH could be captured by a NS within a longer time through multiple oscillations around it. This process is eased if the velocity of the PBHs is small. The authors of Ref. [25] consider NS in the cores of globular clusters, where the velocity dispersion is of order $\mathcal{O}(10)$ km/s, and derive a constraint in the range $M_{\text{PBH}} \sim 10^{-14} - 10^{-10} M_\odot$. The critical assumption that they make concerns the DM density in globular clusters, which is needed to be 10^2 to 10^4 times larger than the average 0.3 GeV/cm^3 in the halo in order to yield a constraint. For more conservative assumptions this bound disappears.

Another bound that we cut at $M_{\text{PBH}} \sim 10^{-11} M_\odot$ comes from the observations with the Hyper Suprime-Cam (HSC) of the Subaru telescope of stars in the Andromeda galaxy M31, at 770 kpc from us. Ref. [23] analysed its data in the search for microlensing events of the stars measured by HSC in the optical window, and derived a constraint in the range $10^{-13} - 10^{-6} M_\odot$.

A first major effect which was unaccounted for in the analysis is the finite size of the sources. The projected size of the main sequence star onto the lensing plane radius is larger by more than order of magnitude than the Einstein radius for PBHs of mass $10^{-11} M_\odot$. Therefore the magnification of the star drops well below 10%, a factor of 10 below what is needed to detect a signal.

Another important phenomenon which further weakens the microlensing constraints below $\sim 10^{-10} M_\odot$ and makes them disappear below $\sim 10^{-11}$ is the so called wave effect [22, 24, 42, 43]. When the observed light has a wavelength λ smaller than the Schwarzschild radius r_s of the lens, then the framework of geometrical optics does not provide a good description of the system, and the diffraction effects give small or vanishing magnification of the source. It is interesting to understand why r_s is a relevant quantity in this discussion, since the deflected images of the source travel at a larger distance $r_E \gg r_s$ from the lens. The explanation is related to the expression of the Einstein radius $r_E \sim \sqrt{r_s D}$. We denote by D the distance between the observer and the lens, which we assume for simplicity to be of the same order as the distance between the lens and the source. One can interpret the travel of the lensed rays at opposite sides of the lens as a double slit interference experiment. The first maxima of the diffracted pattern occur at angles $\theta_1 \sim \lambda/r_E$, where r_E is the equivalent of the distance between the slits. With respect to the line of sight to the PBH, the deflected rays are at an angle $\theta_s \sim r_E/D$. If $\theta_s \gg \theta_1$, then the interference pattern is not resolvable, the wave effects of light diffusion are negligible and the PBH appreciably magnifies the background objects. On the other hand, if $\theta_s < \theta_1$, then the interference pattern is visible, and the geometrical optics approximation breaks down. The condition for magnification $\theta_s \gtrsim \theta_1$ yields $\lambda \lesssim r_E^2/D \sim r_s$.

Because of these reasons, we cut the constraints from the Subaru HSC observations below $M_{\text{PBH}} \sim 10^{-11} M_\odot$.

Appendix B: Computation of \mathcal{D}_{λ_i}

In this Appendix we present the results for the contractions

$$\mathcal{D}_{\lambda_i}(\hat{k}_i, r_i) \equiv e_{ab,\lambda_1}^*(\hat{k}_1) e_{cd,\lambda_2}^*(\hat{k}_2) e_{ef,\lambda_3}^*(\hat{k}_3) \left\{ \left[\vec{q}_a \vec{q}_b (\vec{q} - \hat{k}_1)_c (\vec{q} - \hat{k}_1)_d \vec{q}_e \vec{q}_f \right]_I + [\text{same}]_{II} \right\}, \quad (\text{B.1})$$

where the momenta \vec{k}_i are given in Eq.(3.3), while the momenta $\vec{q}_{I,II}$ are given in Eq.(3.6). We construct the polarization operators as it is standard, following the notation of [38]. We define the two unit vectors orthogonal to the GW momentum through an external fixed unit vector \hat{e}_z , that we choose to be the unit vector along the third axis

$$\hat{u} \equiv \frac{\hat{k} \cdot \hat{e}_z}{|\hat{k} \cdot \hat{e}_z|}, \quad \hat{v} \equiv \hat{k} \cdot \hat{u}. \quad (\text{B.2})$$

⁸ We thank A. Katz for illuminating discussions on the microlensing and neutron star constraints on the PBH abundance.

(clearly, any other fixed vector can equivalently be chosen.) Starting from this choice, we then introduce the left handed and right handed polarization operators

$$e_{ab,R} \equiv \frac{\hat{u}_a + i\hat{v}_a}{\sqrt{2}} \frac{\hat{u}_b + i\hat{v}_b}{\sqrt{2}}, \quad e_{ab,L} \equiv \frac{\hat{u}_a - i\hat{v}_a}{\sqrt{2}} \frac{\hat{u}_b - i\hat{v}_b}{\sqrt{2}}. \quad (\text{B.3})$$

These operators are symmetric, transverse, traceless, and normalized according to $e_{ab,\lambda}^* e_{ab,\lambda} = 1$. They are also related to the operators e_+ , e_- as

$$e_{ab,R/L} = \frac{e_{ab,+} \pm i e_{ab,-}}{\sqrt{2}}. \quad (\text{B.4})$$

The contractions can be readily obtained from these expressions for the polarization operators, and from Eqs.(3.6). The resulting expressions are rather lengthy. We report them here in the isosceles case $r_1 = r_2$, where these expressions acquire a more compact form

$$\begin{aligned} \mathcal{D}_{RRR} = \mathcal{D}_{LLL} &= \frac{1}{256} \left[\frac{32r_1^3}{(2r_1 + r_3)^3} - \frac{24(3r_1^2 + 8)}{(2r_1 + r_3)^2} + \frac{32(r_1^2 + 4)r_3}{r_1^5} + \frac{32(r_1^2 - 1)^2}{r_1^3(2r_1 - r_3)} \right. \\ &\quad \left. + \frac{32(2(r_1^2 + 6)r_1^2 + 9)}{r_1^3(2r_1 + r_3)} - \frac{(r_1^4 + 24r_1^2 + 16)r_3^2}{r_1^6} - \frac{4(33r_1^4 + 24r_1^2 + 16)}{r_1^6} - 32 \right], \\ \mathcal{D}_{LRR} = \mathcal{D}_{RLL} = \mathcal{D}_{RLR} = \mathcal{D}_{LRL} &= \frac{(r_1^2 - 4)^2 (8r_1^4 - 4r_1^2(r_3^2 + 4) + r_3^4 + 4r_3^2)}{256r_1^6(4r_1^2 - r_3^2)}, \\ \mathcal{D}_{RRL} = \mathcal{D}_{LLR} &= \frac{1}{256} \left[-\frac{32r_1^3}{(r_3 - 2r_1)^3} - \frac{24(3r_1^2 + 8)}{(r_3 - 2r_1)^2} - \frac{32(r_1^2 + 4)r_3}{r_1^5} - \frac{32(2(r_1^2 + 6)r_1^2 + 9)}{r_1^3(r_3 - 2r_1)} \right. \\ &\quad \left. + \frac{32(r_1^2 - 1)^2}{r_1^3(2r_1 + r_3)} - \frac{(r_1^4 + 24r_1^2 + 16)r_3^2}{r_1^6} - \frac{4(33r_1^4 + 24r_1^2 + 16)}{r_1^6} - 32 \right]. \end{aligned} \quad (\text{B.5})$$

We note that the contractions are invariant under parity (L \leftrightarrow R). Moreover, we note that LRR = RLR (due to the fact that $r_2 = r_3$).

Appendix C: Redshift

The bispectrum (3.1) can be rewritten as

$$\langle h(\eta, \vec{k}_1) h(\eta, \vec{k}_2) h(\eta, \vec{k}_3) \rangle' = \frac{\hat{B}}{\eta^3}, \quad (\text{C.1})$$

where we have factored out the conformal time η , that accounts for the decrease of the amplitude of the GW mode functions while inside the horizon during radiation domination. Since, in general, the GW amplitude scales as the inverse power of the scale factor inside the horizon, $\langle hhh \rangle \sim 1/a^3$, the bispectrum evaluated today at η_0 is given by:

$$\langle h(\eta_0, \vec{k}_1) h(\eta_0, \vec{k}_2) h(\eta_0, \vec{k}_3) \rangle' = \left(\frac{a_{\text{eq}}}{a_0} \right)^3 \langle h(\eta_{\text{eq}}, \vec{k}_1) h(\eta_{\text{eq}}, \vec{k}_2) h(\eta_{\text{eq}}, \vec{k}_3) \rangle' = \left(\frac{a_{\text{eq}}}{a_0} \right)^3 \frac{1}{\eta_{\text{eq}}^3} \hat{B}, \quad (\text{C.2})$$

where η_{eq} represents the conformal time at the radiation-matter equality. During the radiation-dominated phase the scale factor goes as $a \sim \eta$, and so we can write:

$$a_{\text{eq}} = a_k \cdot \frac{\eta_{\text{eq}}}{\eta_k}, \quad (\text{C.3})$$

where the subscript k denotes the moment at which the comoving momentum k re-enters the horizon. The crossing happens when $k = aH$ such that during the radiation era we have $\eta_k = 1/k = 1/2\pi f$. Appendix G of [21] gives

$$\frac{a_0}{a_k} \sim 2 \cdot 10^{17} \frac{f}{10^{-3}\text{Hz}}, \quad (\text{C.4})$$

that can be used to derive the present bispectrum

$$\langle h(\eta_0, \vec{k}_1)h(\eta_0, \vec{k}_2)h(\eta_0, \vec{k}_3) \rangle' = (\pi \cdot 10^{-20} \text{Hz})^3 \cdot \hat{B}(\vec{k}_1, \vec{k}_2, \vec{k}_3). \quad (\text{C.5})$$

Although in this discussion, for brevity, the equal time bispectrum had been considered, this relation applies also to the unequal time bispectrum considered in the main text.

-
- [1] G. Bertone and T. M. P. Tait, *Nature* **562**, no. 7725, 51 (2018).
- [2] B. P. Abbott et al. [LIGO Scientific and Virgo Collaborations], *Phys. Rev. Lett.* **116**, 061102 (2016) [[gr-qc/1602.03837](#)]
- [3] S. Bird, I. Cholis, J. B. Muoz, Y. Ali-Hamoud, M. Kamionkowski, E. D. Kovetz, A. Raccanelli and A. G. Riess, *Phys. Rev. Lett.* **116**, no. 20, 201301 (2016) [[astro-ph.CO/1603.00464](#)].
- [4] S. Clesse and J. Garca-Bellido, *Phys. Dark Univ.* **15**, 142 (2017) [[astro-ph.CO/1603.05234](#)].
- [5] M. Sasaki, T. Suyama, T. Tanaka and S. Yokoyama, *Phys. Rev. Lett.* **117**, no. 6, 061101 (2016) Erratum: [*Phys. Rev. Lett.* **121**, no. 5, 059901 (2018)] [[astro-ph.CO/1603.08338](#)].
- [6] J. Garca-Bellido, *J. Phys. Conf. Ser.* **840**, no. 1, 012032 (2017) [[astro-ph.CO/1702.08275](#)].
- [7] M. Sasaki, T. Suyama, T. Tanaka and S. Yokoyama, *Class. Quant. Grav.* **35**, no. 6, 063001 (2018) [[astro-ph.CO/1801.05235](#)].
- [8] L. Barack *et al.*, [[gr-qc/1806.05195](#)].
- [9] P. Ivanov, P. Naselsky and I. Novikov, *Phys. Rev. D* **50**, 7173 (1994).
- [10] J. García-Bellido, A.D. Linde and D. Wands, *Phys. Rev. D* **54** (1996) 6040 [[astro-ph/9605094](#)].
- [11] P. Ivanov, *Phys. Rev. D* **57**, 7145 (1998) [[astro-ph/9708224](#)].
- [12] J. R. Espinosa, D. Racco and A. Riotto, *Phys. Rev. Lett.* **120** (2018) no.12, 121301 [[hep-ph/1710.11196](#)].
- [13] I. Musco, [[gr-qc/1809.02127](#)].
- [14] G. Franciolini, A. Kehagias, S. Matarrese and A. Riotto, *JCAP* **1803**, no. 03, 016 (2018) [[astro-ph.CO/1801.09415](#)].
- [15] V. Acquaviva, N. Bartolo, S. Matarrese and A. Riotto, *Nucl. Phys. B* **667** (2003) 119 [[astro-ph/0209156](#)].
- [16] S. Mollerach, D. Harari and S. Matarrese, *Phys. Rev. D* **69** (2004) 063002 [[astro-ph/0310711](#)].
- [17] K. N. Ananda, C. Clarkson and D. Wands, *Phys. Rev. D* **75** (2007) 123518 [[gr-qc/0612013](#)].
- [18] D. Baumann, P. J. Steinhardt, K. Takahashi and K. Ichiki, *Phys. Rev. D* **76** (2007) 084019 [[hep-th/0703290](#)].
- [19] *Prog. Theor. Phys.* **123**, 867 (2010) Erratum: [*Prog. Theor. Phys.* **126**, 351 (2011)] [[astro-ph.CO/0912.5317](#)].
- [20] J. Garcia-Bellido, M. Peloso and C. Unal, *JCAP* **1709**, no. 09, 013 (2017) [[astro-ph.CO/1707.02441](#)].
- [21] N. Bartolo *et al.*, *JCAP* **1612** (2016) no. 12, 026 [[astro-ph.CO/1610.06481](#)].
- [22] A. Katz, J. Kopp, S. Sibiryakov and W. Xue, [[astro-ph.CO/1807.11495](#)].
- [23] H. Niikura *et al.*, [[astro-ph.CO/1701.02151](#)].
- [24] K. Inomata, M. Kawasaki, K. Mukaida and T. T. Yanagida, *Phys. Rev. D* **97**, no. 4, 043514 (2018) [[astro-ph.CO/1711.06129](#)].
- [25] F. Capela, M. Pshirkov and P. Tinyakov, *Phys. Rev. D* **87**, no. 12, 123524 (2013) [[astro-ph.CO/1301.4984](#)].
- [26] T. D. Brandt, *Astrophys. J.* **824**, no. 2, L31 (2016) doi:10.3847/2041-8205/824/2/L31 [[astro-ph.GA/1605.03665](#)].
- [27] T. S. Li *et al.* [DES Collaboration], *Astrophys. J.* **838** (2017) no.1, 8 doi:10.3847/1538-4357/aa6113 [[astro-ph.GA/1611.05052](#)].
- [28] M. Zumalacarregui and U. Seljak, *Phys. Rev. Lett.* **121** (2018) no.14, 141101 [[astro-ph.CO/1712.02240](#)].
- [29] J. Garcia-Bellido, S. Clesse and P. Fleury, *Phys. Dark Univ.* **20** (2018) 95 [[astro-ph.CO/1712.06574](#)].
- [30] N. Bartolo, V. De Luca, G. Franciolini, M. Peloso and A. Riotto, “The Primordial Black Hole Dark Matter - LISA Serendipity,” [[astro-ph.CO/1811.xxxx](#)].
- [31] K. Inomata, M. Kawasaki, K. Mukaida, Y. Tada and T. T. Yanagida, *Phys. Rev. D* **96** (2017) 043504 [[astro-ph.CO/1701.02544](#)].
- [32] D.H. Lyth and A. Riotto, *Phys. Rept.* **314** (1999) 1 [[hep-ph/9807278](#)].
- [33] H. Audley *et al.*, [[astro-ph.IM/1702.00786](#)].
- [34] C. Caprini *et al.*, *JCAP* **1604** (2016) no.04, 001 [[astro-ph.CO/1512.06239](#)].
- [35] J. R. Espinosa, D. Racco and A. Riotto, *JCAP* **1809**, no. 09, 012 (2018) [[hep-ph/1804.07732](#)].
- [36] R. Saito and J. Yokoyama, *Prog. Theor. Phys.* **123**, 867 (2010) Erratum: [*Prog. Theor. Phys.* **126**, 351 (2011)] [[astro-ph.CO/0912.5317](#)].
- [37] E. Bugaev and P. Klimai, *Phys. Rev. D* **81**, 023517 (2010) [[astro-ph.CO/0908.0664](#)].
- [38] N. Bartolo *et al.*, [[astro-ph.CO/1806.02819](#)].
- [39] M. R. Adams and N. J. Cornish, *Phys. Rev. D* **82**, 022002 (2010) [[gr-qc/1002.1291](#)].
- [40] T. L. Smith and R. Caldwell, *Phys. Rev. D* **95** (2017) no.4, 044036 [[gr-qc/1609.05901](#)].
- [41] P. W. Graham, S. Rajendran and J. Varela, *Phys. Rev. D* **92** (2015) no.6, 063007 [[hep-ph/1505.04444](#)].
- [42] A. Gould, Submitted to: *Astrophys. J. Lett.* (1991).
- [43] T. T. Nakamura, *Phys. Rev. Lett.* **80** (1998) 1138.
- [44] N. Cornish and T. Robson, [[astro-ph.HE/1803.01944](#)].
- [45] M.J. Hinich, *Journ. of Time Series Analysis*, vol. **3**, 169 (1982).

- [46] M.J. Hinich and G.R. Wilson, IEEE Transactions on Acoustics, Speech, and Signal Processing, vol. **38**, 7 (1990).
- [47] N. Bartolo, V. De Luca, G. Franciolini, M. Peloso and A. Riotto, in preparation.
- [48] R. g. Cai, S. Pi and M. Sasaki, [[astro-ph.CO/1810.11000](https://arxiv.org/abs/1810.11000)].